Article

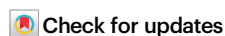# Ultrasensitive dim-light neuromorphic vision sensing via momentum-conserved reconfigurable van der Waals heterostructure

Check for updates

Lei Xu[1,6], Junling Liu[1,6], Xinrui Guo[1], Shuo Liu[1], Xilin Lai[1], Jingyue Wang [2], Mengshi Yu[2], Zhengdao Xie[3], Hailin Peng [2], Xuming Zou [3], Xinran Wang [4], Ru Huang [1] & Ming He [1,5] ✉

Reconfigurable phototransistors featuring bipolar photoresponses are favorable for manipulating high-performance neuromorphic vision sensory. Here, we present a momentum-conserved reconfigurable phototransistor based on the van der Waals heterojunction between methylammonium lead iodide perovskite and two-dimensional Bi_2O_2Se semiconductor, which exhibits a synergistic interplay of interband hot-carrier transitions and reconfigurable heterointerface band alignments, eventually achieving the ultrahigh bipolar optoelectronic performances with the photoresponsivity of 6×10^7 AW^{-1}, accompanied by the specific detectivity of 5.2×10^{11} Jones, and the dynamic range of 110 dB. Moreover, A 3×3 heterotransistor array is fabricated to perform in-sensor analog multiply-accumulate operations even under the challenging dim illumination of 0.1 μWcm^{-2} that comparable to natural moonlight. The reconfigurable heterotransistor array can be further adopted to enhance the traffic-light detection under dim-light conditions. Our advancement in momentum-conserved reconfigurable heterotransistor signifies a leap forward in real-time, energy-efficient, and low-light image processing for neuromorphic vision sensors.

Bioinspired neuromorphic vision (NV) sensor offers a compelling opportunity to reduce data shuttling, latency, and energy consumption by directly assigning specific computing tasks inside the sensor[1–3], thus gaining significant interests in the fields of intelligent robotics, surveillance security, and industrial automation. At their core, NV sensors mimic the roles of photoreceptor and bipolar cells in the human retina[4], where photoreceptor cells transform incoming light into electrical signals, followed by the signal preprocessing of bipolar cells in an on/off framework to extract image features as illustrated in Fig. 1a. Similarly, the photoresponse of NV sensors can be analogized to the magnitude and direction of information flow in bipolar cells: a positive response implies an incline of target activations triggered by the source stimulus, while a negative response indicates a decline[5]. Notably, negative photoresponses play an important role in nullifying specific features, offsetting certain inputs, thereby allowing NV sensors to adeptly process complex interrelationships. Therefore, embedding

[1]Beijing Advanced Innovation Center for Integrated Circuits, School of Integrated Circuits, Peking University, Beijing, China. [2]Beijing National Laboratory for Molecular Sciences, College of Chemistry and Molecular Engineering, Peking University, Beijing, China. [3]Key Laboratory for Micro/Nano Optoelectronic Devices of Ministry of Education, School of Physics and Electronics, Hunan University, Changsha, China. [4]National Laboratory of Solid State Microstructures, School of Electronic Science and Engineering, Nanjing University, Nanjing, China. [5]Frontiers Science Center for Nano-optoelectronics, Peking University, Beijing, China. [6]These authors contributed equally: Lei Xu, Junling Liu. ✉e-mail: minghe@pku.edu.cn
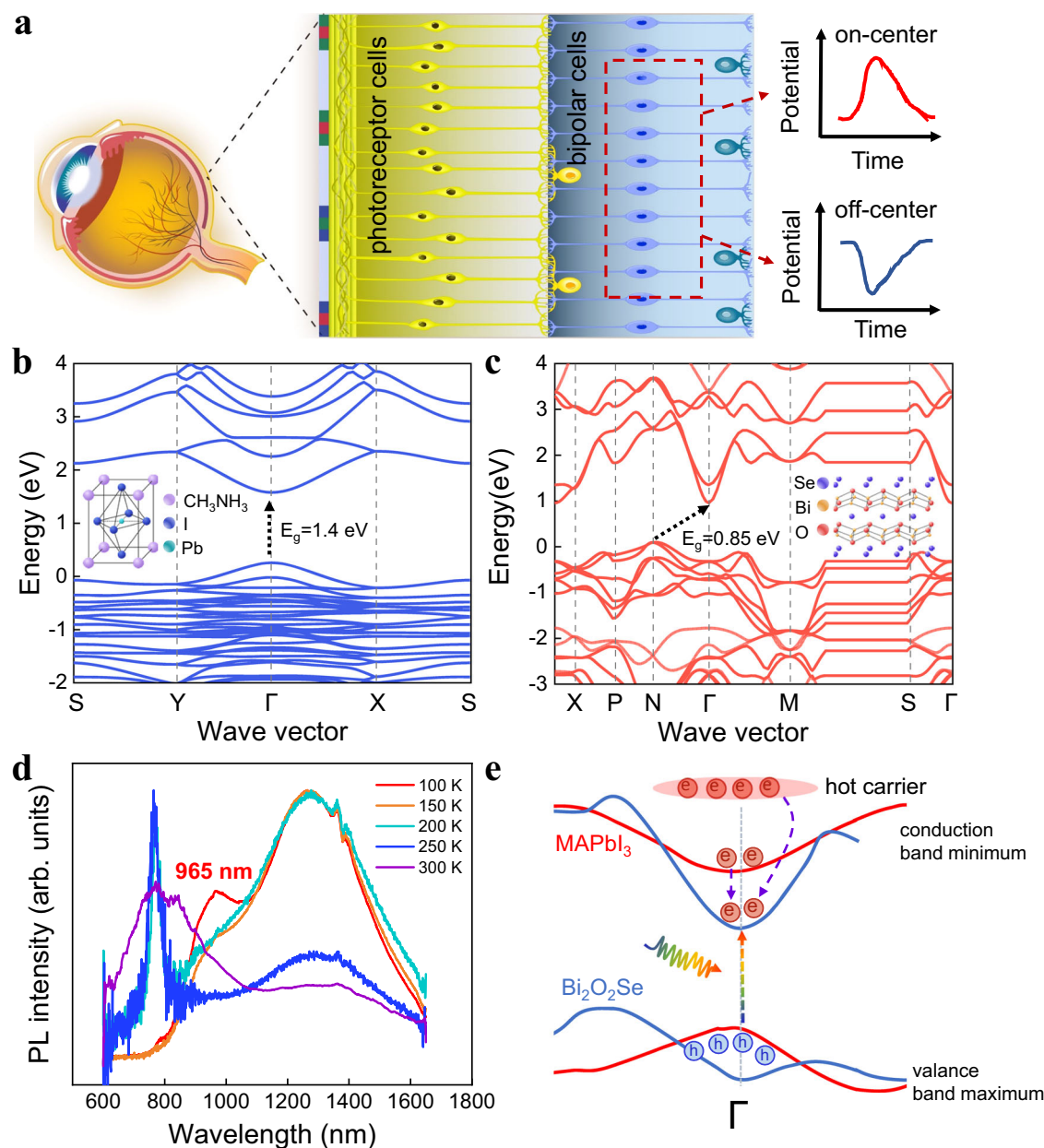
Fig. 1 | Reconfigurable neuromorphic vision sensing and momentum conservation. a Schematic illustration of the human retina consisting of photoreceptor and bipolar cells for vision information processing via the on/off framework. Energy band structure of **b** $MAPbI_3$, and **c** Bi_2O_2Se calculated by the density functional theory. **d** Temperature-dependent steady-state photoluminescence (PL) spectra of the $MAPbI_3/Bi_2O_2Se$ heterojunction. **e** Diagram of the interband photoexcitation and hot-carrier transition in the momentum-conserved $MAPbI_3/Bi_2O_2Se$ heterojunction.

bipolar optoelectronic functionalities in a single device is pivotal for in-sensor edge processing such as feature extraction, pattern classification, and motion tracking.

Very recently, both positive and negative photoelectrical responses have been manifested in two-dimensional (2D) van der Waals (vdW) heterostructure phototransistors, which are regulated by external gate biases, photogating effects, and ferroelectric fields[6,7]. Since thinner films are favored for better electric-field manipulations, 2D bipolar phototransistors often suffer from suboptimal optoelectronic performances in terms of narrow wavelength range, low photoresponsivity, and small signal-to-noise ratio (SNR), resulting in remarkably limited recognition precisions in complex real world, especially for dim-light scenarios. In contrast, halide perovskites endowed with direct bandgaps possess robust absorption capabilities

irrespective of film thicknesses. The conduction-band bottom of halide perovskites originates from the degenerated Pb 6p orbitals with a narrow dispersion, leading to a high density of states[8]. Unfortunately, the inherent ion migrations in halide perovskites substantially screen the carrier transport[9], consequently restricting the photoconductive gains.

Beyond the absorption loss, high-energy hot carriers above the band edge induce ~30% loss to the optoelectronic efficiency in the form of thermalization[10]. These hot carriers typically undergo ultrafast relaxations through the carrier-phonon scatterings within femtosecond timescales, preceding their arrival at the band edge for extractions[11]. Thus, it is imperative that the extraction rate of hot carriers can compete with the cooling rate. In fact, semiconductors with spatial confinements, including quantum dots, nanowires, and nanofilms, exhibit

decelerated hot-carrier cooling due to strong Coulomb interactions[12], substantial exciton-binding energies[13], and diminished electron-phonon couplings[14]. Intriguingly, halide perovskites have recently been spot-lighted as promising hot-carrier absorbers with slow cooling rates, ascribed to the pronounced hot-phonon bottleneck effect stemming from nonequilibrium longitudinal-optical (LO) phonons[15]. Integrating halide perovskites within 2D vdW heterojunctions might harness a synergistic effect of hot-carrier extractions and tunable band align-ments, which could pave the way for the simultaneous capacitation of enhanced optoelectronic sensing and neuromorphic computing. However, effective hot-carrier extractions from such an integrated heterostructure have rarely been explored.

Herein, we rationally manufacture a momentum-conserved vdW heterostructure capable of ultrasensitive bipolar photoresponses. The momentum conservation between methylammonium lead iodide ($MAPbI_3$) perovskite and 2D Bi_2O_2Se semiconductor is demonstrated to significantly promote hot-carrier extractions and interlayer carrier transports at the reconfigurable $MAPbI_3$/Bi_2O_2Se heterojunction, leading to an ultrahigh photoresponsivity of 6×10^7 AW^{-1}, accom-panied by a specific detectivity of 5.2×10^{11} Jones, and a dynamic range of 110 dB. Moreover, we fabricate Bi_2O_2Se/$MAPbI_3$ heterotransistor arrays in the size of 3×3 that effectively performed in-sensor analog multiply-accumulate (MAC) operations to extract key image features under the challenging illumination of moonlight (i.e., $0.1 \mu W$ cm^{-2}). The phototransistor arrays are further employed in convolutional neural networks (CNNs) to improve the detection of traffic lights under dim-light environments and deliver remarkable recall rates of 99.2%, 95.8%, and 92.6% for green, red, and yellow signals, respectively.

Results and discussion

Momentum conservation for hot-carrier transitions

Theoretical insights have suggested that the momentum conservation of energy band levels could facilitate interband hot-carrier extractions[16,17]. Recently, we have demonstrated Bi_2O_2Se as an emer-ging 2D semiconductor that is characterized by its distinctive electronic-ionic layered structure with ultrahigh carrier mobility[18-20]. In addition, the $[Bi_2O_2]_n^{2n+}$ layer adopts 2D square lattices that are structurally compatible with perovskite crystals[21], making it an ideal candidate for assisting the carrier transport of halide perovskites. In this context, the density functional theory (DFT) was employed to calculate the band structures of $MAPbI_3$ and Bi_2O_2Se (Supplementary Note 1). Figure 1b reveals that $MAPbI_3$ possesses a direct bandgap (E_g) of ~1.4 eV with its conduction-band minimum (CBM) and valence-band maximum (VBM) both located at the Γ point. Conversely, Bi_2O_2Se exhibits an indirect bandgap of ~0.8 eV, bridging the VBM at the N point and the CBM at the Γ point (Fig. 1c). In particular, the VBM and CBM of $MAPbI_3$, alongside the CBM of Bi_2O_2Se, all reside at the Γ point, indicating that these band levels are momentum conserved[22]. This theoretical alignment was further experimentally verified through the temperature-dependent steady-state photoluminescence (PL) spectra (Fig. 1d), wherein the emerging peak at 965 nm was correlated with the interband transfer between the VBM of $MAPbI_3$ and the CBM of Bi_2O_2Se (i.e., ~1.28 eV), affirming the momentum-matched bandgap at the heterojunction interface. This founding signifies that the $MAPbI_3$/Bi_2O_2Se heterojunction is primed for interband photocarrier transi-tions as illustrated in Fig. 1e: the momentum conservation between the VBM of $MAPbI_3$ and the CBM of Bi_2O_2Se allows direct photoexcitation from the perovskite layer into the high-mobility Bi_2O_2Se channel, while the momentum-conserved CBMs facilitate hot-carrier extractions from $MAPbI_3$ to Bi_2O_2Se. Taking together, both are anticipated to markedly boost the photosensing efficiency of $MAPbI_3$/Bi_2O_2Se heterostructure.

$MAPbI_3$/Bi_2O_2Se heterostructured phototransistors were manu-factured in the architecture of back-gated field-effect transistors as depicted in Fig. 2a. An ultrathin Bi_2O_2Se layer (i.e., ~5 nm) was adopted

for effective gate modulations, while the $MAPbI_3$ thickness (i.e., ~140 nm) was optimized to amplify photon absorption. The cross-sectional high-resolution transmission electron microscopy (HRTEM) in Fig. 2b displays a clear interface between $MAPbI_3$ and Bi_2O_2Se domains. Notably, the single-crystal Bi_2O_2Se layer exhibited a body-centered tetragonal structure, closely adjoining the tetragonal per-ovskite crystals with micrometer-sized grains (Supplementary Fig. 1)[23]. This crystalline compatibility is beneficial for crafting a high-quality $MAPbI_3$/Bi_2O_2Se heterojunction that is important for acquiring super-ior optoelectronic behaviors. Figure 2c shows that the $MAPbI_3$/Bi_2O_2Se heterotransistor reached excellent mobility exceeding 300 cm^2 V^{-1} s^{-1} with a high on/off ratio of 10^7, underscoring the successful establish-ment of premium $MAPbI_3$/Bi_2O_2Se heterojunction.

$MAPbI_3$/Bi_2O_2Se heterojunction film exhibits excellent light absorptions in the broadband visible-NIR spectrum of 300–1500 nm (Supplementary Fig. 2). Photocarrier dynamics at the $MAPbI_3$/Bi_2O_2Se heterojunction were probed using time-resolved photoluminescence spectroscopy as shown in Fig. 2d. The observed photocarrier decay kinetics align well with the two-body recombination model, indicating the non-geminate recombination is predominated within $MAPbI_3$[24]. The heterojunction displayed an accelerated photocarrier decay rate (i.e., $\tau_1 = 11 \pm 1$ ns and $\tau_2 = 91 \pm 3$ ns) as compared with that of $MAPbI_3$ (i.e., $\tau_1 = 68 \pm 2$ ns and $\tau_2 = 271 \pm 5$ ns), validating the fast photocarrier transfer from $MAPbI_3$ to Bi_2O_2Se that ascribed to the momentum conservation between the CBMs of $MAPbI_3$ and Bi_2O_2Se. Furthermore, femtosecond transient absorption (fs-TA) spectroscopy was employed to scrutinize the hot-carrier dynamics, and a pump photon energy of 3.1 eV (i.e., 1.5 eV above the bandgap of $MAPbI_3$) with a low pump fluence of $1 \mu J$ cm^{-2} was used to avoid the non-radiative Auger recombination[25]. Figure 2e, f shows the pseudocolor fs-TA plots of $MAPbI_3$ and $MAPbI_3$/Bi_2O_2Se heterojunction films, respectively. Within the initial 0.1 ps after photoexcitation, a negative photoinduced absorption (PIA) band centered at 1.58 eV (i.e., the blue region) appeared in both films, which was ascribed to the hot-carrier induced bandgap renormalization. As the PIA band decayed with a blue shift disclosed in the normalized fs-TA spectra (Fig. 2g), a positive ground-state photobleaching (GSB) band centered at 1.65 eV (i.e., the red region) with a high-energy tail extended to 2.0 eV (i.e., the white region) became apparent, further confirming the population of high-energy hot carriers[26,27]. The high-energy tail of GSB band was observed to reach thermal equilibrium within 1.2 ps, and its decay dynamics can be elucidated by tracking the temporal profile of hot-carrier tem-perature (T_c). Since the energy of GSB tail is far above the band edge, the hot-carrier distribution can be approximated to the Maxwell–Boltzmann distribution, and then the T_c is derived from: $\Delta A(E) = -A_0(E) \exp(-\frac{E}{k_B T_c})$, where ΔA is the transient absorbance, k_B is the Boltzmann constant[28]. Figure 2h compares the hot-carrier cool-ing curves of $MAPbI_3$ and $MAPbI_3$/Bi_2O_2Se heterojunction films. The inherent polar nature of $MAPbI_3$ results in an exponential decline in T_c, primarily driven by the electron-LO-phonon scatterings. In particular, the heterojunction exhibited an increased cooling rate with T_c drop-ping to ~1500 K within 0.3 ps after photoexcitation as compared that of ~1800 K in $MAPbI_3$, indicating efficient extractions of high-energy photocarriers from $MAPbI_3$ into Bi_2O_2Se anchored on the momentum conservation between their respective CBMs. The relatively modest exciton binding energy (i.e., 19 ± 3 meV) suggests the simultaneous presence of excitons and free carriers at the band edge of $MAPbI_3$ at room temperature[29], and the absence of obvious Moss-Burstein shift in the GSB peak of 1.65 eV implies that the decay dynamics of $MAPbI_3$ and $MAPbI_3$/Bi_2O_2Se heterojunction films at the band edge are probably dominated by exciton quenching to free carriers[24,26]. In addition, Fig. 2i reveals an accelerated decay rate for the GSB peak within the $MAPbI_3$/Bi_2O_2Se heterojunction along the timescale of 600 ps, providing more evidence on the effective photocarrier extractions at the momentum-conserved heterojunction.
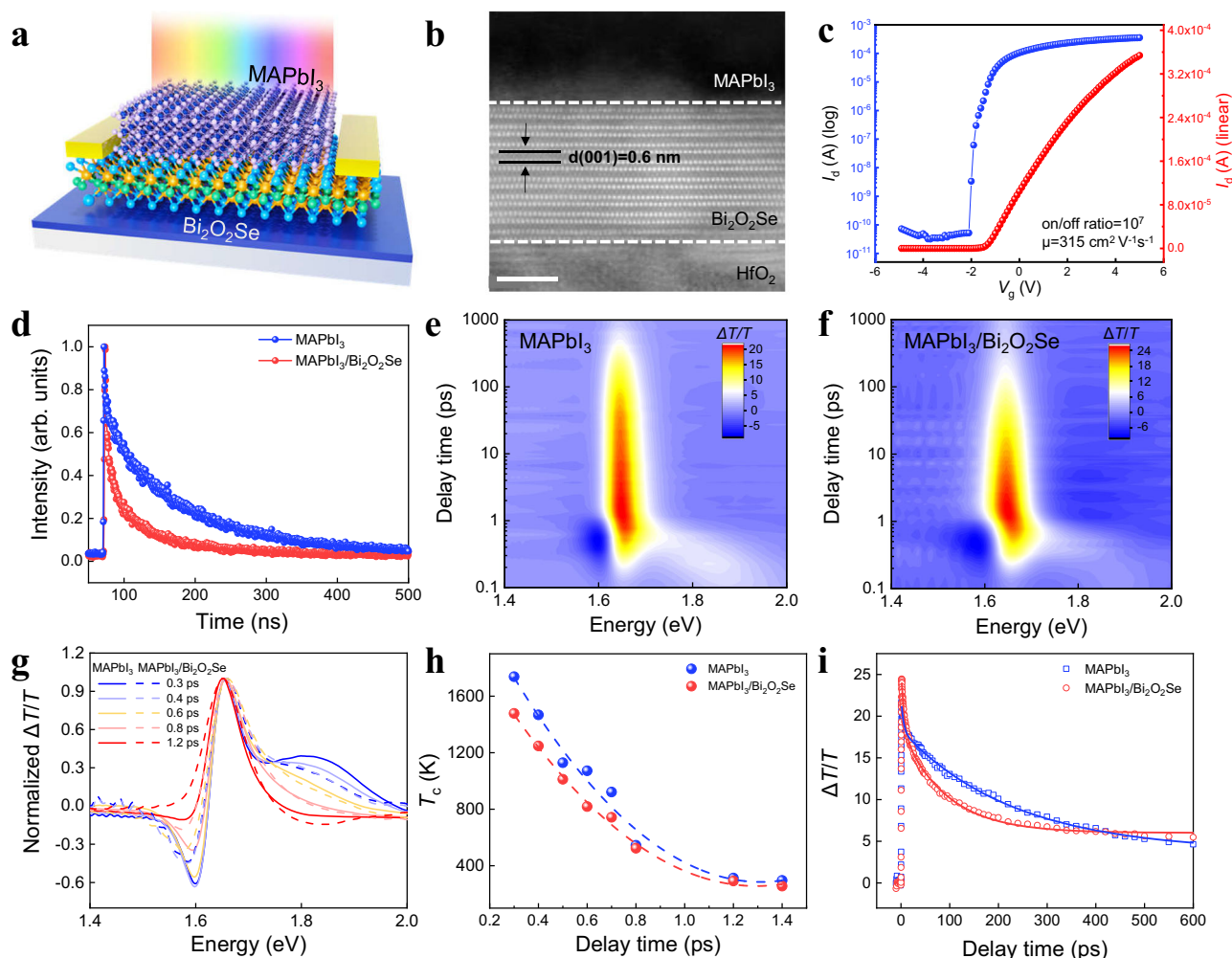
Fig. 2 | Momentum conservation facilitates hot-carrier transitions. a Illustration of the MAPbI$_3$/Bi$_2$O$_2$Se heterojunction-based field-effect transistor (FET) for neuromorphic vision sensing. **b** Cross-sectional high-resolution transmission electron microscopy (HRTEM) image of the MAPbI$_3$/Bi$_2$O$_2$Se heterojunction. The scale bar is 2 nm. **c** Typical transfer curves of MAPbI$_3$/Bi$_2$O$_2$Se heterojunction-based FETs. **d** Time-resolved photoluminescence (TRPL) spectroscopy of MAPbI$_3$ and MAPbI$_3$/Bi$_2$O$_2$Se heterojunction films upon the light excitation of 470 nm. Pseudocolor femtosecond transient absorption (fs-TA) plots of **e** MAPbI$_3$, and **f** MAPbI$_3$/Bi$_2$O$_2$Se heterojunction. **g** Normalized fs-TA spectra of MAPbI$_3$ and MAPbI$_3$/Bi$_2$O$_2$Se heterojunction films within the 1.2 ps after the photoexcitation. **h** Decay dynamics of the hot-carrier temperature within MAPbI$_3$ and MAPbI$_3$/Bi$_2$O$_2$Se heterojunction films. **i** Decay dynamics of the ground-state photobleaching band peaks at 1.65 eV within MAPbI$_3$ and MAPbI$_3$/Bi$_2$O$_2$Se heterojunction films.

Ultrasensitive gate-tunable bipolar photoresponses

Significantly enhanced photocarrier transitions at the MAPbI$_3$/Bi$_2$O$_2$Se heterojunction driven by the momentum conservation anticipates a remarkable boost in the optoelectronic efficiencies of the heterotransistors. Figure 3a presents the transfer curves of MAPbI$_3$/Bi$_2$O$_2$Se heterotransistors under the illumination of 532 nm with varied light intensities. Positive photoresponses were observed at the V_g below 0.5 V, as the light-induced source-drain photocurrent surpassed the dark current. Conversely, the heterotransistors rendered negative photoresponses beyond this V_g threshold as shown in Fig. 3b. Remarkably, the photoresponsivity (R) defined as $R = I_{ph}/P$ exceeded the order of 10^6 AW^{-1} for both positive and negative responses, outstripping its MAPbI$_3$ and Bi$_2$O$_2$Se counterparts (Supplementary Fig. 3), where I_{ph} is the net photocurrent, and P is the incident light intensity.

The specific detectivity (D^*) is determined by $D^* = \frac{R\sqrt{A\Delta f}}{i_n}$, where A is the effective detection area, Δf is the operational bandwidth, and i_n is the noise current. The noise spectrum of MAPbI$_3$/Bi$_2$O$_2$Se heterotransistor at varied gate voltages was characterized (Supplementary Fig. 4). An remarkable R of 6×10^7 A/W was achieved accompanied with a D^* of 5.2×10^{11} Jones and an external quantum efficiency (EQE) of 1.2×10^8%, marking a pronounced advancement of optoelectronic performances over prior bipolar photosensors[2,30,31]. More impressively, the heterotransistors consistently delivered high R values over a broad light-intensity range from 0.1 μW cm^{-2} to 30 mW cm^{-2} following a sublinear relationship on the logarithmic scale (Fig. 3c). This led to an expansive dynamic range (DR) of 110 dB defined by DR $= 20 \times \log(\frac{P_{max}}{P_{min}})$[32], where P_{max} is the maximum light intensity corresponding to the measured maximum photocurrent, and P_{min} is the minimum one, thus reinforcing its versatile applicability across diverse optoelectronic applications from bright sunlight to dim moonlight.

Bipolar photoresponses of MAPbI$_3$/Bi$_2$O$_2$Se heterotransistors can be modulated by adjusting the gate voltage throughout the visible spectrum (Supplementary Fig. 5). The mapping plots of bipolar photoresponses as a function of the gate voltage as well as the incident light intensity at the wavelengths of 532 nm, 640 nm, and 780 nm are depicted in Fig. 3d and Supplementary Fig. 6, providing a full framework to implement varied photoresponsivities in NV sensors to update the weights for in-sensor convolutional operations[33]. Figure 3e displays
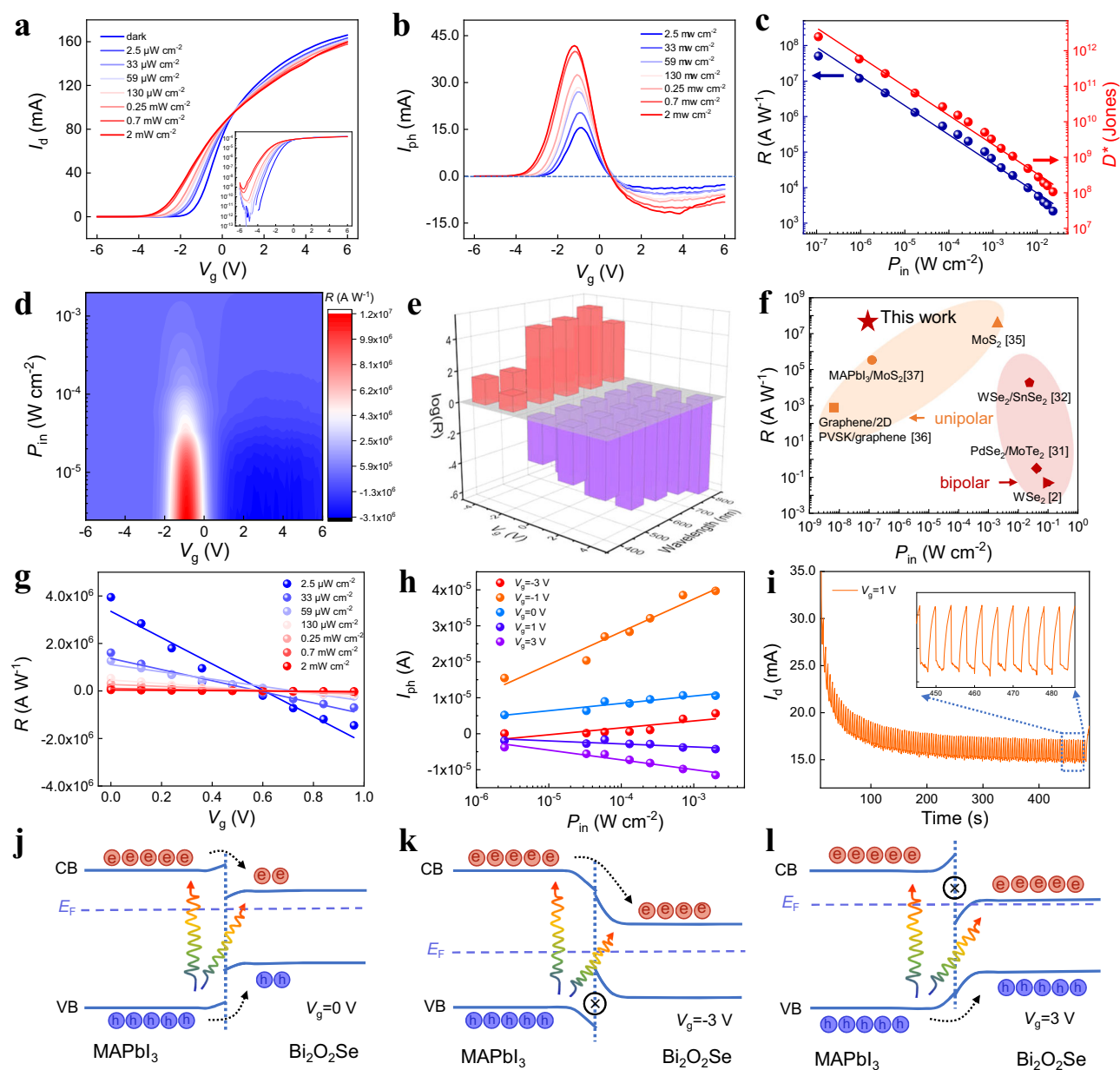
Fig. 3 | Photoresponse characterization of reconfigurable MAPbI$_3$/Bi$_2$O$_2$Se heterotransistors. a Transfer curves and **b** net photocurrents of MAPbI$_3$/Bi$_2$O$_2$Se heterotransistor under 532 nm illumination with varied light intensities. **c** Light-intensity dependence of the photoresponsivity R and the specific detectivity D^* under 532 nm illumination at the gate voltage of 0 V. **d** Pseudo-color plot of the photoresponsivity under 532 nm illumination with varied light intensities, in which the gate voltage was tuned from −6 to 6 V. **e** Dependence of bipolar photoresponsivity on the gate voltage in the visible illumination range of 400–800 nm.

f Benchmark of the photoresponsivity in various unipolar and bipolar photosensors. **g** Linear dependence of the bipolar photoresponsivity on the gate voltage under 532 nm illumination. **h** Dependence of the net photocurrent on the light intensity under 532 nm illumination with the gate voltage varying from −3 to 3 V. **i** Photocurrent curves measured under the on/off recycles for negative photoresponses. **j**–**l** Illustration of band alignment and interlayer carrier transfer of the MAPbI$_3$/Bi$_2$O$_2$Se heterotransistor under the gate voltage of 0 V, −3 V, and 3 V, respectively.

that the photoresponsivity of heterotransistors maintained at a high-level ranging from 10^3 AW^{-1} to 10^6 AW^{-1} for both positive and negative photoresponses across the visible spectrum of 400–800 nm, demonstrating robust sensitivities for detecting a broad range of colorful images. Figure 3f benchmarks the photoresponsivity of bipolar photosensors crafted from various low-dimensional materials with diverse architectures[2,30,31,34–36], wherein the MAPbI$_3$/Bi$_2$O$_2$Se heterotransistor markedly achieved the highest value.

In addition, the linear dependency of bipolar photoresponses on gate voltages across the visible spectrum is depicted in Fig. 3g and Supplementary Fig. 7. This linear relationship allows the direct employment of positive and negative bipolar photoresponsivity as

CNN weights by adjusting gate voltages. The photocurrent of our heterotransistor photodetectors exhibited sublinear dependences on the light intensity on the logarithmic scale (Fig. 3h and Supplementary Fig. 8). This logarithmic sublinear photoresponse prevents the saturation under high light intensities, similar to human eyes, allowing the device to effectively perceive both bright and dark images[37]. Moreover, we comprehensively analyzed both the photoresponsivity and photocurrent of all nine devices within the 3 × 3 MAPbI$_3$/Bi$_2$O$_2$Se heterotransistor array under 640 nm illumination (Supplementary Figs. 9 and 10), revealing that the maximum positive photoresponsivity was consistent in the range of $(2.4 \pm 0.9) \times 10^5$ AW^{-1} and the maximum negative one maintained in the range of $(−4.8 \pm 1.1) \times 10^5$ AW^{-1}

(Supplementary Figs. 11a, b). In addition, all the nine devices within the heterotransistor array maintained uniform photocurrents at varied gate voltages under both low and high light intensities (Supplementary Figs. 11c, d). We also subjected the devices to the stability testing. At the very beginning, all the nine devices in the array exhibited uniform bipolar photoresponses (Supplementary Figs. 12 and 13). After storing in an ambient environment (i.e., $27 \pm 1\,^{\circ}\mathrm{C}$ and $55 \pm 5\,\%$ humidity) for 168 h (i.e., one week), all devices mostly maintained the bipolar behavior (Supplementary Figs. 14 and 15). It is noteworthy that critical challenges of ensuring the long-term stability of $MAPbI_3$ perovskite, maintaining the uniformity of film qualities, and preventing defects during the film transfer process must be addressed to achieve large-scale productions. In addition, the device photoresponse to continuous light pulses was tested under different gate voltages, confirming their excellent reproducibility (Fig. 3i and Supplementary Fig. 16). The response time for negative photoresponses was characterized in the magnitude order of 10 ms that comparable to those of biological bipolar cells[38], whereas the response time for positive photoresponses maintained in the magnitude order of 100 ms (Supplementary Fig. 17).

To elucidate the physical mechanisms for the gate-tunable bipolar photoresponses in the $MAPbI_3/Bi_2O_2Se$ heterojunction, ultraviolet photoelectron spectroscopy was employed to determine the VBM and Fermi level (E_F) of $MAPbI_3$, which were identified as -5.6 eV and -4.2 eV, respectively (Supplementary Fig. 18). The optical bandgap of $MAPbI_3$ was measured to be 1.6 eV by steady-state photoluminescence spectrum, thus yielding the $MAPbI_3$ CBM of -4.0 eV. Similarly, the VBM, CBM, and E_F of Bi_2O_2Se were characterized at -5.0 eV, -4.2 eV, and -4.3 eV, respectively[39]. Thus, a type-I band alignment is proposed for the $MAPbI_3/Bi_2O_2Se$ heterojunction in Fig. 3j, where the conduction band offset ΔE_c and the valance band offset ΔE_v are calculated to be 0.2 eV and 0.6 eV. When subjected to a negative V_g, the electrostatic-doping effect is expected to downshift the E_F of both Bi_2O_2Se and $MAPbI_3$, promoting the formation of a p-n junction at the heterointerface as depicted in Fig. 3k. In this configuration, an increased ΔE_v restricts the hole transport, while a negligible ΔE_c favors the electron transport into the Bi_2O_2Se channel, resulting in positive photoresponses. In addition, the direct photoexcitation of electrons from the VBM of $MAPbI_3$ to the CBM of Bi_2O_2Se due to the momentum conservation will further enhance the positive photoresponses[40]. In the case subjected to a positive V_g, the E_F of $MAPbI_3$ approaches its CBM, leading to an n-n type contact with Bi_2O_2Se as illustrated in Fig. 3l. This configuration elevates the ΔE_c, impedes the electron transport from $MAPbI_3$ to Bi_2O_2Se, facilitates the hole injection into the Bi_2O_2Se channel, and eventually yields negative photoresponses. It is noteworthy that the ambipolar feature of $MAPbI_3$ perovskite plays a crucial role in modifying the band alignment via the electrostatic gating[41], allowing for the modulation between p-n junction (i.e., positive photoresponses) and n-n junction (i.e., negative photoresponses) in the $MAPbI_3/Bi_2O_2Se$ heterojunction.

Dim-light neuromorphic vision sensing

The $MAPbI_3/Bi_2O_2Se$ heterotransistor array in the size of 3×3 was fabricated as shown in Fig. 4a. The detailed manufacturing process is schemed in Supplementary Fig. 19. The photocurrents through the $MAPbI_3/Bi_2O_2Se$ heterotransistor surpassed those through the singular perovskite device by at least three orders of magnitude (Supplementary Figs. 20a–c). Photocurrent mapping further confirms the significantly high photocurrent intensity within the $MAPbI_3/Bi_2O_2Se$ heterojunction zone in comparison to adjacent regions (Supplementary Fig. 20d). This indicates that the predominant photocurrent conduction occurs through the $MAPbI_3/Bi_2O_2Se$ domain, whereby the large electrical resistance and minimal photoresponse of the intervening perovskite layer between pixels act as effective barriers against photocurrent leakages. This array merges the biological functions of

photoreceptor and bipolar cells, wherein the photosensing efficiency is enhanced by the momentum-conserved interlayer hot-carrier transfer, while the gate-tunable band alignment paves the way for reconfigurable MAC operations, facilitating the extraction of key image features as illustrated in Fig. 4b, c. In particular, the photo-responsivity R_{ij} of each heterotransistor can be swayed to either positive or negative directions by applying the corresponding gate voltage V_{ij}, drawing parallels with updating weights in neural networks. The photocurrents generated from each line are then collectively integrated across the array, adhering to the Kirchhoff's law[33], to execute in-sensor MAC operations of $I_{out} = \sum_{i,j}^{i=3,j=3}(I_{ph})_{ij} = \sum_{i,j}^{i=3,j=3} R_{ij} \times P_{ij} = I_d - I_{d0}$, where I_d is the readout current of the array under illumination, and I_{d0} is the readout dark current of the array. Indeed, the photoresponsivity emerges as one of major factors that influences the capability of NV sensory under complex environments. A high-photoresponsivity amplifies photocurrents under dim-light conditions, eliminating the need for additional gain circuits and the associated energy costs for signal boosting. These augmented photocurrents increase resistances against signal noises, ensuring the accuracy of in-sensor data processing. In quantifying the energy consumption of the heterotransistor throughout a singular light pulse episode, we suppose the energy consumption into two principal components: the energy E_1 requisite for sustaining the photoresponsivity as $E_1 = V_g \times I_g \times T_{duration}$, where V_g is the gate voltage essential for sustaining the photoresponsivity, I_g is the gate current, and $T_{duration}$ is the duration of single light pulse operation; and the energy E_2 inherent to the in-sensor computing function as $E_2 = I_{light} \times V_{ds} \times T_{duration}$. Employing the $T_{duration}$ parameter set at 100 ms, we estimate the energy consumption spans from 10^{-3} to 1 nJ dependent on the varied gate voltages.

To evaluate the sensory capability of our ultrasensitive heterotransistor array, it was assigned to the practical task of classifying the letters of "P", "K", and "U" under the dim-light intensity of $0.1\,\mu W\,cm^{-2}$, which was comparable to that of natural moonlight (Supplementary Note 2). Figure 4d schemes the training process of the reconfigurable heterotransistor array with varied bipolar photoresponsivities in the magnitude order of $10^2\,AW^{-1}$, $10^4\,AW^{-1}$, and $10^6\,AW^{-1}$, respectively. The detailed training algorithm is charted in Supplementary Fig. 21. For each training epoch, total of 210 Gaussian-noised letters were optically projected onto the heterotransistors for training. Through the one-hot encoding approach[42], each letter was programmed to activate single output node. The softmax function $S(I_{out}) = \frac{e^{I_{out}}}{\sum_{k=1}^{3} e^{R_k P_k}}$ was utilized as the activation function[43], denoting the probability of each letter falling into the class k. After each epoch n, the R_{ij}^n was updated via the gradient backpropagation of the loss function $R_{ij}^{n+1} = R_{ij}^n - \frac{\eta}{M}\sum_P \nabla_{R_{ij}^n}\psi$, where η is the learning rate, M is the total number of projected letters, ψ is the loss function $\psi = -\frac{1}{k}\sum_{k=1}^{3} y_m \log[S(I_{out})]$, and y_m is the label[44]. We note that the updated photoresponsivity R_{ij}^{n+1} was practically implemented in the heterotransistors by adjusting V_g according to the mapping plot in Fig. 3d.

As the number of training epoch increased, each R_{ij} of the heterotransistor array was progressively refined, ultimately enabling the identification of target letter when its average output current exceeded that of the other two (Fig. 4e and Supplementary Fig. 22). Notably, the high-photoresponsivity heterotransistor in the magnitude order of $10^6\,AW^{-1}$ readily yielded amplified readout photocurrents without the need of extra denoising circuits, thus conferring a high SNR as compared with that of low-photoresponsivity ones. An elevated SNR ensures accurate data acquisition, empowering the device to effectively process visual information even in dim-light environments. Figure 4f, g compares the loss function and the corresponding recognition accuracy of phototransistor arrays with varied
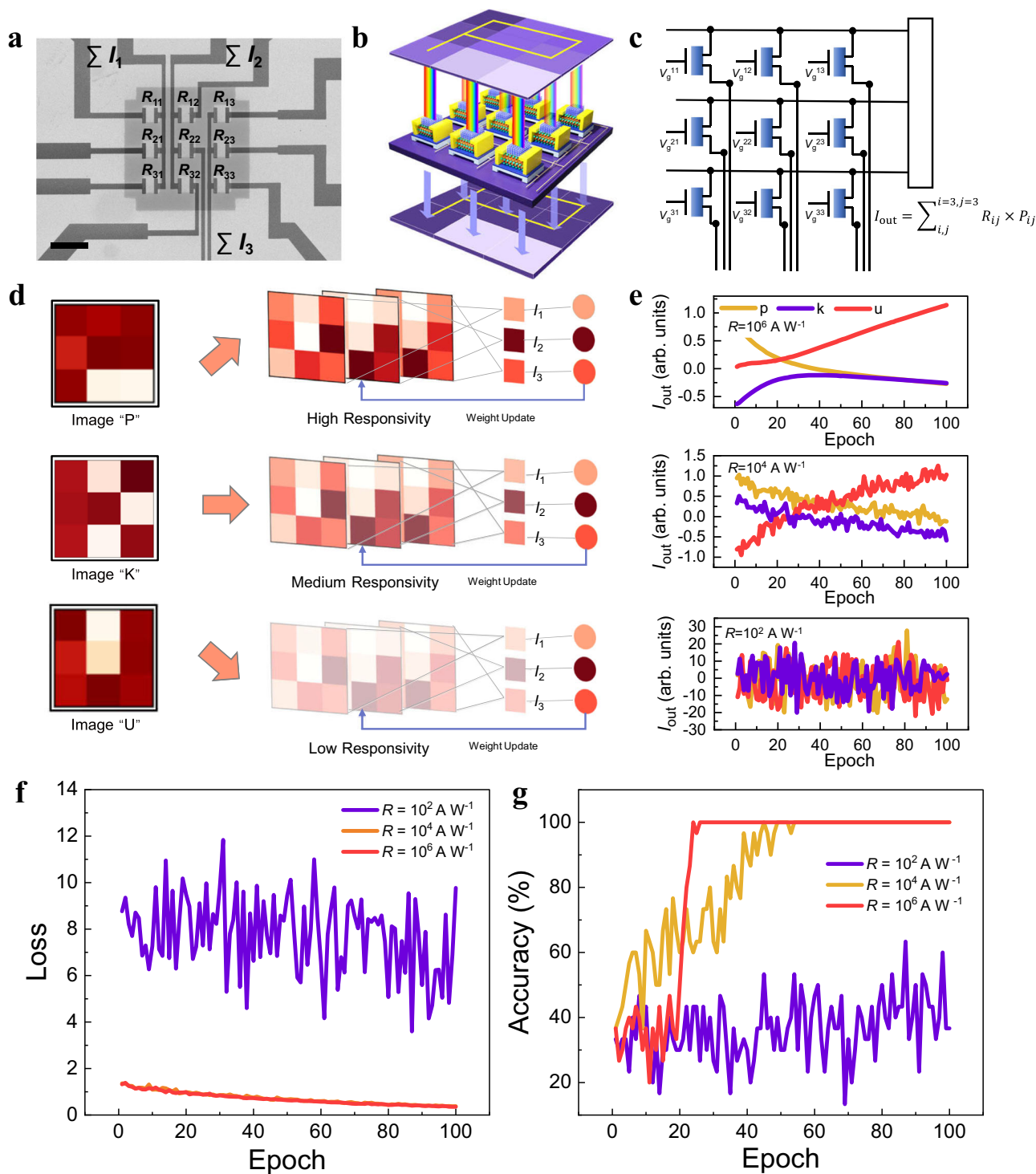
Fig. 4 | Implementation of the heterotransistor array for dim-light classification. a Scanning electron microscopy (SEM) image of as-fabricated MAPbI$_3$/Bi$_2$O$_2$Se heterotransistor array. The scale bar is 10 μm. **b** Illustration of the reconfigurable heterotransistor array adapted for in-sensor neural network computing. **c** Schemed circuit for in-sensor analog multiply-accumulate operations. **d** Training flow of classifying the letters of "P", "K", and "U" under the dim-light intensity of 0.1 μW cm^{-2} by using the heterotransistor arrays with various photoresponsivities. **e** Output photocurrents of the heterotransistor arrays with various photoresponsivities executing in-sensor analog multiply-accumulate operations for classifying the letter "U". **f** Loss and **g** recognition accuracy for various photoresponsivities over the epoch.

photoresponsivities. The low photoresponsivity in the magnitude order of 10^2 AW^{-1} induced pronounced fluctuations in both loss functions and recognition accuracies that impeded letter classifications. In contrast, the heterotransistors with the photoresponsivity in the magnitude order of 10^4 AW^{-1} demonstrated a swift decline in the loss function, and attained a 100% recognition accuracy after 50 training epochs, which further decreased to 20 epochs for the high photoresponsivity in the magnitude order of 10^6 AW^{-1}, largely minimizing the response time for real-time visual classification tasks.

The heterotransistor array can serve as an in-sensor convolution kernel to extract key features of a full visual image (Supplementary Note 3). According to the Kirchhoff's law, a full image was sequentially

projected through the kernel to divide into 3×3 sub-images to perform the convolution operation, and each sub-I_{out} was reconstructed to generate the kernel-processed image with enhanced features. Benefiting from the ultrasensitive bipolar photoresponses of MAPbI$_3$/Bi$_2$O$_2$Se heterotransistors, a diverse set of tunable photoresponse weights can be implemented within the 3×3 kernel to proficiently process image data. As exampled in Fig. 5a, the convolution kernels for Gaussian, Inverse, and Laplacian operators were experimentally implemented in the heterotransistor array to complete the image processing of noise reduction, image stylization, and edge detection, respectively[45]. The pixel data of a dim-light image captured at Peking University were converted to optical signals, and then projected onto the heterotransistors, wherein specific configurations of Gaussian, Inverse, and Laplacian operators were deployed with their respective V_g values. All operators were successfully processed on the dim-light images. The ultrasensitive heterotransistor array produced more detailed edges of the stone lion and the school gate under the dim-light condition, and the edge-detection entropy of highly responsive heterotransistor array (i.e., $R = 2 \times 10^6$ AW^{-1}) was 1.9×10^{-3} compared with that of 1.5×10^{-5} for low-responsive one (i.e., $R = 5 \times 10^4$ AW^{-1}), indicating that more effective information was extracted from the image by the high-photoresponsivity heterotransistors.

To evaluate the effect of varying photoresponsivity levels on image processing, we configured the array into Laplacian convolution kernels by adjusting the gate voltages. As shown in Supplementary Fig. 23, the high-responsivity configurations successfully detected edges in both bright and dim images, whereas the low-responsivity configurations led to significant edge information loss in dim images. The ultrasensitive reconfigurable heterotransistor array holds promises for improving dim-light visual perception in CNNs[2,46]. In this regard, the heterotransistor array was interconnected with the YOLOv4 neural network to detect traffic lights from complex surroundings[47,48]. In the preprocessing of traffic-light images, each of the RGB channels underwent individual processing facilitated by a 3×3 bipolar phototransistor array that serves as a Gaussian filter. This approach involved the application of distinct wavelength and bias parameters to each channel, meticulously configured to optimize the convolution and denoising phases of image preprocessing. Dim-light images sourced from LISA Traffic Lights Dataset were interfered with Gaussian noises (i.e., standard deviation of 0.2) to serve as deteriorated raw images, which were then projected onto the reconfigurable heterotransistors to emulate simultaneous sensing and preprocessing with convolution kernels. The resultant I_{out} was transformed back into pixel data and fed into the YOLOv4 neural network for further training and detection tests as illustrated in Fig. 5b. The presence of noise within RGB imagery precipitates the blurring of details and the distortion of color fidelity (Supplementary Fig. 24). Conversely, the application of denoising process facilitates the restoration of visual clarity and intricacy, a transformation underscored by the histogram evolution from the homogenously smooth distribution to one characterized by multiple peaks. The integration of denoising into the preprocessing regimen significantly elevates the quality of the image, simultaneously expediting the training convergence of neural network. This efficiency gain is attributed to the diminished necessity for the network to adaptively learn the exclusion of noise artifacts, thereby streamlining the computational process and enhancing the overall performance of the neural network in machine-learning applications. The precision-recall curves of the preprocessed images demonstrated excellent recalls of 99.2%, 95.8%, and 92.6% for green, red, and yellow lights, respectively, as compared with those of 89.1%, 72.6%, and 65.2% from raw images (Fig. 5c and Supplementary Fig. 25). The mean average precision of traffic-light detection was improved from 73.2 to 95.9% by adopting the preprocessing as seen in Fig. 5d, validating the in-sensor processing effectiveness of reconfigurable MAPbI$_3$/Bi$_2$O$_2$Se heterotransistors with excellent optoelectronic photoresponses.

In conclusion, we have demonstrated the cutting-edge reconfigurable NV sensor based on the MAPbI$_3$/Bi$_2$O$_2$Se heterostructure, wherein the momentum conservation between MAPbI$_3$ perovskite and 2D Bi$_2$O$_2$Se semiconductor plays a crucial role in facilitating interlayer hot-carrier transitions, setting up a benchmark with the bipolar photoresponsivity of 10^7 AW^{-1}, the specific detectivity of 10^{11} Jones, and the dynamic range of 110 dB. By adopting these ultrasensitive bipolar photoresponses as CNN weights, the heterotransistors have been tailored to execute reconfigurable in-sensor convolution operations. This capability enables proficient early visual processing tasks even under the challenging dim illumination of 0.1 μW cm^{-2} reminiscent of natural moonlight conditions, obviating the need for additional gain circuits and the associated energy consumptions. Our work marks the significant advancement towards highly sensitive, energy-efficient, and in-sensor neuromorphic sensors. Distinguished by its high responsiveness and in-sensor computing capabilities, the MAPbI$_3$/Bi$_2$O$_2$Se heterotransistor presents a promising avenue for creating systems that boast improved performance and functionality when integrated with neural networks or various electronic components.

Methods

Device fabrications

The devices were manufactured in the architecture of back-gate field-effect transistors. Bi$_2$O$_2$Se films were grown on a mica substrate by chemical vapor deposition, followed by transferring to HfO$_2$/silicon substrates using the poly(methyl methacrylate)-assisted method. To fabricate a patterned Bi$_2$O$_2$Se array, a 3×3 mask was applied with electron beam lithography (Raith, Voyager) to define the channel pattern, and then the exposed areas were etched by argon plasma (Leuven Instruments, LCCP–6A reactive ion etcher). The source and drain electrodes (Pd/Au=5/60 nm) were deposited using a combination of standard electron-beam lithography (Raith, Voyager), electron-beam evaporation (DETECH, DE400), and lift-off processes. The substrate hydrophilicity was enhanced by subjecting it to a slight treatment with oxygen plasma (Harrick plasma, PDC-002). Subsequently, the solution of methylammonium lead iodide perovskite dissolved in dimethylformamide was spin-coated onto the substrate, followed by the anti-solvent treatment with chlorobenzene, and then the films were thermally annealed at 100 °C for 15 min under N$_2$ atmosphere.

Device characterizations and electrical measurements

Cross-sectional transmission electron microscopy (TEM) specimens were prepared using an in situ focused ion beam (FIB) lift-out technique. Time-resolved photoluminescence (TRPL) spectroscopy was performed on an Edinburgh Instruments spectrometer (FLS 1000) with a 468 nm excitation light source. High-resolution imaging was subsequently captured by spherical aberration-corrected TEM (Thermo, Themis Z) operating at an accelerating voltage of 200 kV. Femtosecond transient absorption (fs-TA) spectroscopy was characterized by using a commercial spectrometer (Light conversion, harpia/pharos). The pump photon energy was set to 3.1 eV (i.e., 400 nm) with the intensity of 1 μJ cm^{-2}. Time-resolved fs-TA spectrum was scanned from 2.07 eV (i.e., 600 nm) to 1.46 eV (i.e., 850 nm) with a temporal resolution of 100 fs. Electrical characterizations were conducted using a probe station (Lakeshore, CRX-VF) equipped with an Agilent B1500A semiconductor parameter analyzer. Incident illuminations with varied light intensities were processed using a 532 nm (CNI, MDL-III-780 nm), 640 nm (CNI, MDL-III-780 nm), and 780 nm laser (CNI, MDL-III-780 nm), and the power density was measured by a power meter (Newport, 843-R).

Implementation of pattern classification

The task of classifying the letters "P", "K", "U" is executed using Multilayer Perceptron (MLP) model. In this task, the architecture encompasses an input layer furnished with 9 neurons $(x_1, x_2, \ldots, x_9)$,
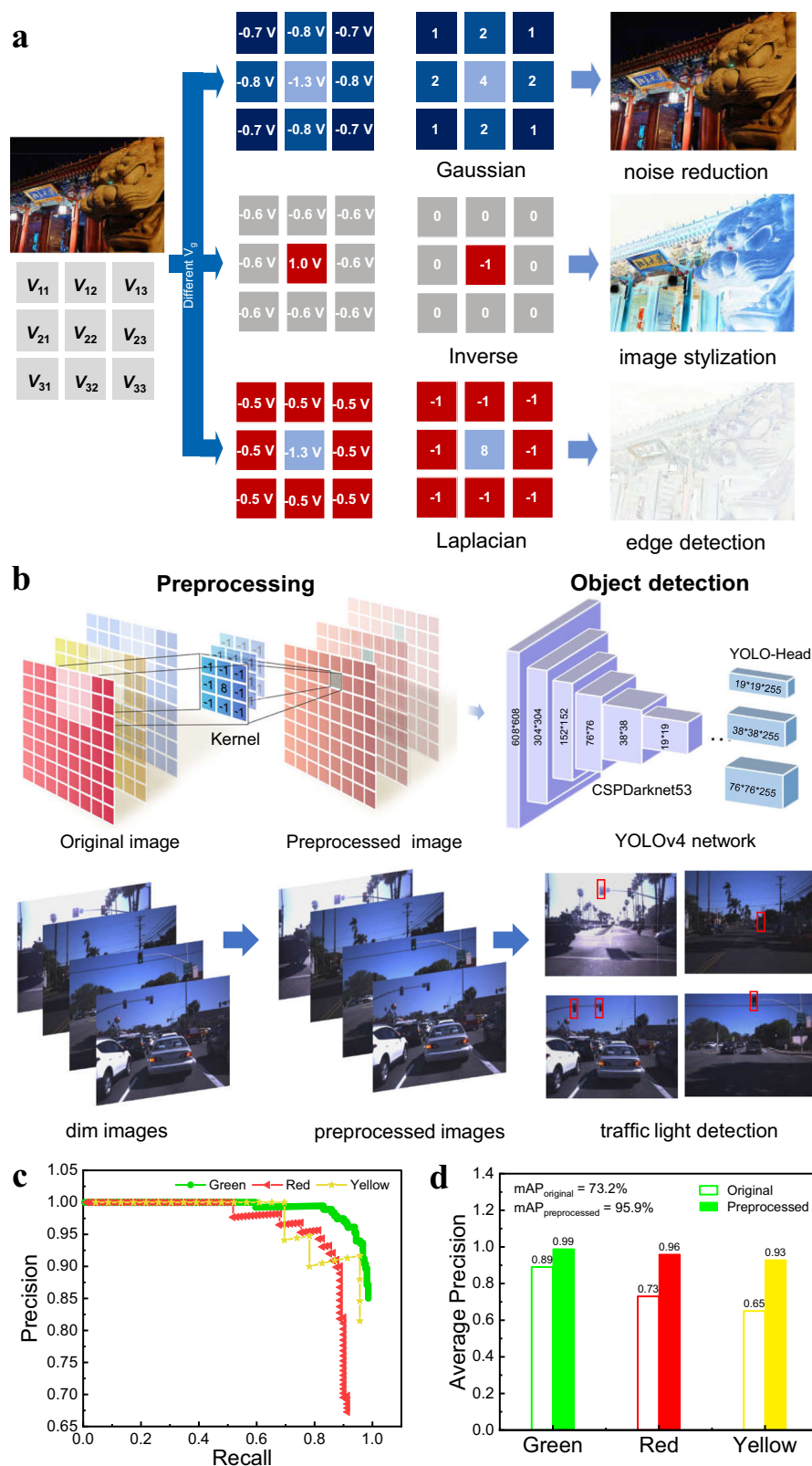
Fig. 5 | Ultrasensitive dim-light neuromorphic vision sensing. a Implementation of Gaussian, Laplacian, Inverse operators in the MAPbI$_3$/Bi$_2$O$_2$Se heterotransistor array for the image processing of noise reduction, edge detection, and image stylization, respectively. **b** Scheme of integrating the MAPbI$_3$/Bi$_2$O$_2$Se heterotransistor array with the YOLOv4 network for the traffic-light detection task under dim-light conditions. **c** Recall–precision curves of green, red, and yellow traffic lights preprocessed by the heterotransistor array under dim-light conditions. **d** Mean average precisions (*mAP*) of the raw and the preprocessed images for green, red, and yellow traffic lights.

mirroring the 9-pixel values of the input letter image, and culminates in an output layer with 3 neurons (y_P, y_K, y_U), each dedicated to one of the target letters. The interconnection between input and output strata is facilitated via a weight matrix W with the output neuron activation a_j determined by $a_j = \sum_{i=1}^{9} W_{ij} \cdot x_i + b_j$, where W_{ij} is the weight from the input neuron i to the output neuron j, and b_j is the bias term for the output neuron j. This configuration enables the precise recognition of letters, as the network discriminates based on the highest activation value among the output neurons.

In a typical hardware realization, this neural construct can be emulated using an array of bipolar sensors, epitomizing in-sensor computing. In this work, the photoresponsivity R_{ij} of MAPbI$_3$/Bi$_2$O$_2$Se heterotransistor array are tailored through the gate voltage $V_{g_{ij}}$ to reflect the synaptic weights W_{ij} of a neural network. Upon exposure to light encoding the input data P_{ij}, each device in the array generates a photocurrent I_{ij} proportional to the product of the input signal and its responsivity: $I_{ij} = R_{ij} \cdot P_{ij}$. The total current output $I_{out} = \sum_{i,j}^{i=3,j=3} I_{ij} = \sum_{i,j}^{i=3,j=3} R_{ij} \cdot P_{ij}$, embodies the multiply-accumulate (MAC) operation within the sensor array, harnessing Kirchhoff's law to execute computation.

For the classification task, a specialized dataset comprising 100 instances of Gaussian-noise afflicted "P", "K", and "U" letter patterns (i.e., noise standard deviation of 0.2) is segmented into training and testing sets in a 7:3 ratio. The letters are illuminated onto the sensor array with peak incident light intensity set at $0.1 \, \mu W \, cm^{-2}$. Comparative analysis is conducted across three sensor arrays, differentiated by the photoresponsivity of $10^2 \, AW^{-1}$, $10^4 \, AW^{-1}$, and $10^6 \, AW^{-1}$, respectively. The photoresponsivity of each heterotransistor is initialized randomly at the beginning. The projection of the letter image induces a readout current $I_{out} = \sum_{i,j}^{i=3,j=3} I_{ij} = \sum_{i,j}^{i=3,j=3} R_{ij} \cdot P_{ij}$, which is activated by the softmax function $S(I_{out}) = \frac{e^{\xi I_{out}}}{\sum_{k=1}^{3} e^{\xi \cdot R_k P_k}}$, where k is the elements within the "P", "K", "U" set, and ξ is the scaling factor. By integrating impacts of noise and hysteresis into our simulation, and to elucidate the effects of different responsiveness on recognition accuracy, a Gaussian noise with the variance of 0.003 was deployed on the readout photocurrent. A loss function $\psi = -\frac{1}{k} \sum_{k=1}^{3} y_m \log[S(I_{out})]$ is defined to quantify the error for training, where y_m is the label of each input letter. Through iterative training, employing the backpropagation algorithm with a learning rate of 0.001, the photoresponsivity R_{ij} of each sensor in the array is fine-tuned by modulating the gate voltage V_g, thereby minimizing the loss function and enhancing classification accuracy. It is worth noting that, due to the device-to-device variations in the array, which are significant non-ideal factors in neuromorphic computing, we edited the photoresponsivity-gate voltage (R–V_g) data measured from the nine devices into a lookup table. This enables us to accurately simulate the conductance modulation process of these devices.

Data availability
The data supporting the findings of this study are available within the article and its Supplementary Information files. All other relevant raw data can be obtained from the corresponding author upon request.

References
1. Liu, K. Q. et al. An optoelectronic synapse based on α-In$_2$Se$_3$ with controllable temporal dynamics for multimode and multiscale reservoir computing. *Nat. Electron.* **5**, 761–773 (2022).
2. Mennel, L. et al. Ultrafast machine vision with 2D material neural network image sensors. *Nature* **579**, 62–66 (2020).
3. Huang, P. Y. et al. Neuro-inspired optical sensor array for high-accuracy static image recognition and dynamic trace extraction. *Nat. Commun.* **14**, 6736 (2023).
4. Liao, F. Y. et al. Bioinspired in-sensor visual adaptation for accurate perception. *Nat. Electron.* **5**, 84–91 (2022).
5. Zhang, Z. H. et al. All-in-one two-dimensional retinomorphic hardware device for motion detection and recognition. *Nat. Nanotechnol.* **17**, 27–32 (2022).
6. Liu, R. et al. Band alignment engineering in two-dimensional transition metal dichalcogenide-based heterostructures for photodetectors. *Small Struct.* **2**, 20000136 (2021).
7. Fang, H. H. & Hu, W. D. Photogating in low dimensional photodetectors. *Adv. Sci.* **4**, 1700323 (2017).
8. Tao, S. X. et al. Absolute energy level positions in tin-and lead-based halide perovskites. *Nat. Commun.* **10**, 8420 (2019).
9. Kim, T. et al. Mapping the pathways of photo-induced ion migration in organic-inorganic hybrid halide perovskites. *Nat. Commun.* **14**, 1846 (2023).
10. Nelson, C. A., Monahan, N. R. & Zhu, X. Y. Exceeding the Shockley-Queisser limit in solar energy conversion. *Energy Environ. Sci.* **6**, 3508–3519 (2013).
11. Nie, Z. G. et al. Ultrafast carrier thermalization and cooling dynamics in few-layer MoS$_2$. *ACS Nano* **8**, 10931–10940 (2014).
12. Gamble, J. K., Friesen, M., Joynt, R. & Coppersmith, S. N. Cooling of cryogenic electron bilayers via the Coulomb interaction. *Phys. Rev. B.* **84**, 125321 (2011).
13. Wang, L. et al. Slow cooling and efficient extraction of C-exciton hot carriers in MoS$_2$ monolayer. *Nat. Commun.* **8**, 13906 (2017).
14. Esmaielpour, H. et al. Enhanced hot electron lifetimes in quantum wells with inhibited phonon coupling. *Sci. Rep.* **8**, 12473 (2018).
15. Fu, J. H. et al. Hot carrier cooling mechanisms in halide perovskites. *Nat. Commun.* **8**, 1300 (2017).
16. Chen, Y. Z., Li, Y. J., Zhao, Y. D., Zhou, H. Z. & Zhu, H. M. Highly efficient hot electron harvesting from graphene before electron-hole thermalization. *Sci. Adv.* **5**, eaax9958 (2019).
17. Yu, H. Y., Wang, Y., Tong, Q. J., Xu, X. D. & Yao, W. Anomalous light cones and valley optical selection rules of interlayer excitons in twisted heterobilayers. *Phys. Rev. Lett.* **115**, 187002 (2015).
18. Tan, C. W. et al. 2D fin field-effect transistors integrated with epitaxial high-gate oxide. *Nature* **616**, 66–72 (2023).
19. Cai, Q. F. et al. Sub-10mK-resolution thermal-bolometric integrated FET-type sensors based on layered Bi$_2$O$_2$Se semiconductor nanosheets. In *2020 IEEE International Electron Devices Meeting (IEDM)*, **26**, 24 (IEEE, 2020).
20. Wu, J. X. et al. High electron mobility and quantum oscillations in non-encapsulated ultrathin semiconducting Bi$_2$O$_2$Se. *Nat. Nanotechnol.* **12**, 530–534 (2017).
21. Chen, C. et al. Electronic structures and unusually robust bandgap in an ultrahigh-mobility layered oxide semiconductor Bi$_2$O$_2$Se. *Sci. Adv.* **4**, eaat8355 (2018).
22. Özçelik, V. O., Azadani, J. G., Yang, C., Koester, S. J. & Low, T. Band alignment of two-dimensional semiconductors for designing heterostructures with momentum space matching. *Phys. Rev. B.* **94**, 035125 (2016).
23. Zhu, Z. Y., Yao, X. P., Zhao, S., Lin, X. & Li, W. B. Giant modulation of the electron mobility in semiconductor Bi$_2$O$_2$Se via incipient ferroelectric phase transition. *J. Am. Chem. Soc.* **144**, 4541–4549 (2022).
24. Manser, J. S. & Kamat, P. V. J. N. P. Band filling with free charge carriers in organometal halide perovskites. *Nat. Photonics* **8**, 737–743 (2014).
25. Xing, G. et al. Long-range balanced electron-and hole-transport lengths in organic-inorganic CH$_3$NH$_3$PbI$_3$. *Science* **342**, 344–347 (2013).

26. Yang, Y. et al. Observation of a hot-phonon bottleneck in lead-iodide perovskites. *Nat. Photonics* **10**, 53–59 (2016).

27. Price, M. B. et al. Hot-carrier cooling and photoinduced refractive index changes in organic-inorganic lead halide perovskites. *Nat. Commun.* **6**, 8420 (2015).

28. Li, M. J. et al. Slow cooling and highly efficient extraction of hot carriers in colloidal perovskite nanocrystals. *Nat. Commun.* **8**, 14350 (2017).

29. Sun, S. Y. et al. The origin of high efficiency in low-temperature solution-processable bilayer organometal halide hybrid solar cells. *Energy Environ. Sci.* **7**, 399–407 (2014).

30. Pi, L. et al. Broadband convolutional processing using band-alignment-tunable heterostructures. *Nat. Electron.* **5**, 248–254 (2022).

31. Ghosh, S. et al. n. Polarity-tunable photocurrent through band alignment engineering in a high-speed $WSe_2/SnSe_2$ diode with large negative responsivity. *ACS Nano* **16**, 4578–4587 (2022).

32. Fang, Y. J., Armin, A., Meredith, P. & Huang, J. S. Accurate characterization of next-generation thin-film photodetectors. *Nat. Photonics* **13**, 1–4 (2019).

33. Zhou, F. C. & Chai, Y. Near-sensor and in-sensor computing. *Nat. Electron.* **3**, 664–671 (2020).

34. Dodda, A. et al. Active pixel sensor matrix based on monolayer MoS_2 phototransistor array. *Nat. Mater.* **21**, 1379–1387 (2022).

35. Tian, H., Wang, X., Wu, F., Yang, Y. & Ren, T.-L. High performance 2D perovskite/graphene optical synapses as artificial eyes. In *2018 IEEE International Electron Devices Meeting (IEDM)* **38**, 34 (IEEE, 2018).

36. Wang, Y. et al. Solution-processed MoS_2/organolead trihalide perovskite photodetectors. *Adv. Mater. Process.* **29**, 1603995 (2017).

37. Pierre, A., Gaikwad, A. & Arias, A. C. Charge-integrating organic heterojunction phototransistors for wide-dynamic-range image sensors. *Nat. Photonics* **11**, 193–199 (2017).

38. Walston, S. T., Chow, R. H. & Weiland, J. D. Direct measurement of bipolar cell responses to electrical stimulation in wholemount mouse retina. *J. Neural Eng.* **15**, 046003 (2018).

39. Luo, P. et al. Self-driven WSe_2/Bi_2O_2Se Van der Waals heterostructure photodetectors with high light on/off ratio and fast response. *Adv. Funct. Mater.* **31**, 2008351 (2021).

40. Chen, Y. F. et al. Momentum-matching and band-alignment van der Waals heterostructures for high-efficiency infrared photodetection. *Sci. Adv.* **8**, eabq1781 (2022).

41. Qin, K. et al. Perovskite/InGaZnO-based reconfigurable optoelectronic device. *IEEE. Electr. Device L.* **43**, 1929–1932 (2022).

42. Rodríguez, P., Bautista, M. A., Gonzàlez, J. & Escalera, S. Beyond one-hot encoding: lower dimensional target embedding. *Image Vision. Comput.* **75**, 21–31 (2018).

43. Rawat, W. & Wang, Z. H. Deep convolutional neural networks for image classification: a comprehensive review. *Neural Comput.* **29**, 2352–2449 (2017).

44. Rumelhart, D. E., Hinton, G. E. & Williams, R. J. Learning representations by back-propagating errors. *Nature* **323**, 533–536 (1986).

45. Karniadakis, G. E. et al. Physics-informed machine learning. *Nat. Rev. Phys.* **3**, 422–440 (2021).

46. Wang, C. Y. et al. Gate-tunable van der Waals heterostructure for reconfigurable neural network vision sensor. *Sci. Adv.* **6**, eaba6173 (2020).

47. Wang, C. Y., Bochkovskiy, A. & Liao, H. Y. M. Scaled-YOLOv4: scaling cross stage partial network. In *2021 IEEE/CVF Conference on Computer Vision and Pattern Recognition, CVPR 2021*. 13024–13033 (IEEE, 2021).

48. Roy, A. M., Bose, R. & Bhaduri, J. A fast accurate fine-grain object detection model based on YOLOv4 deep neural network. *Neural Comput. Appl.* **34**, 3895–3921 (2022).

Acknowledgements

Author contributions

M.H. conceived the original idea for the project. L.X., S.L., X.L., X.G., J.W., Z.X., X.Z., and X.W. contributed to the device fabrication, characterization, electronic measurement and analysis. J.L. carried out the simulation. S.L., M.Y., and H.P. synthesized Bi_2O_2Se nanosheets. The manuscript was written by M.H. and L.X. with inputs from the other authors. M.H. and R.H. directed the research. All authors contributed to the scientific planning and discussion.

Competing interests

The authors declare no competing interests.

Additional information

Supplementary information The online version contains supplementary material available at https://doi.org/10.1038/s41467-024-53268-4.

Correspondence and requests for materials should be addressed to Ming He.

Peer review information *Nature Communications* thanks Saptarshi Das, Cheng-Yan Xu and Xiaodong Yan for their contribution to the peer review of this work. A peer review file is available.

Reprints and permissions information is available at http://www.nature.com/reprints

Publisher's note Springer Nature remains neutral with regard to jurisdictional claims in published maps and institutional affiliations.